Small Signal Analysis of a Grid-Forming Modular Multilevel Converter with a Novel Virtual Synchronous Generator Control

Chen. Jiang, Ajinkya. D. Sinkar and Aniruddha M. Gole

***Abstract*—This paper introduces a grid forming (GFM) control method – detailed synchronous machine emulation virtual synchronous generator (VSG). The proposed method makes a voltage source converter exactly emulate a synchronous generator (SG), using a current source interface. The precise emulation of an SG gives tighter control over overcurrent and improved transient damping. Electromagnetic Transients (EMT) simulation is used to demonstrate the operation, and small signal model is used to assess the stability performance. Small signal analysis shows that the resulting VSG operates stably, and oscillatory modes can be damped by appropriate optimization of the virtual damping windings resistances.**

***Keywords*: Electromagnetic Transients (EMT) Simulation, Grid Forming (GFM) Converter, Modular Multilevel Converter (MMC), Small Signal Model, Virtual Synchronous Generator (VSG) Control.**

I. Introduction

VOLTAGE source converters (VSCs) are increasingly being used in modern power grids for interconnecting renewable energy sources (RES), distributed energy resources (DER) and high-voltage dc (HVdc) transmission [1]-[2]. Since R. Marquardt developed the modular multilevel converter (MMC) in 2005 [3], this type of converter is fast becoming the preferred VSC topology due to the lower power loss and near-sinusoidal output waveform that eliminates the need for additional filtering. Nowadays, the MMC is widely used in applications such as HVdc transmission [4], variable-speed drives [5], wind turbine generators [6], flexible ac transmission systems (FACTS) [7] and so on.

Typically, the VSC control mode can be either the grid following (GFL) or grid forming (GFM) type. In the GFL mode, a phase-locked loop (PLL) is used to track the phase of the system voltage waveform and generate the reference signal for generating the on/off signals for the VSC's IGBT switches. On the other hand, the GFM itself generates its output waveform and can be used for connecting to passive loads or very weak systems. With high penetration of RES and DER, a GFL converter becomes very susceptible to ac voltage changes, as the PLL's tracking capacity becomes compromised [8]. To improve the transient response and steady-state stability, the GFM is proposed. The Virtual synchronous generator (VSG) is one possible GFM control strategy, in which the converter is controlled to mimic the behaviour of a synchronous generator (SG). In most cases, a simplified model of the SG is used, as in the 'synchronverter' [9], where the electro-mechanical swing equation and a simplified representation of damping are included. Additional blocks, such as an extra damping loop [10] can be added to such a model to improve dynamic performance. Similarly, a virtual impedance controller can be combined with the VSG representation to emulate the slow time-varying (quasi-stationary) impedance characteristic of a real SG [11][12]. These type of controllers typically provide d- and q-axis current orders which can be passed to a decoupled dq controller to generate the modulation index for the converter's firing pulse generation block. A current limiting feature, to prevent damage to valves can be embedded into such a controller by adding suitable limits to the dq current orders. However, [13] shows that such an 'embedded' current controller may cause the GFM converter to become unstable when connected to a strong system.

In this paper, a novel current-controlled VSG, which emulates the mechanical and electrical dynamics of an actual SG is incorporated. Reference [14] introduced the basic algorithm and compared its operation with a simple swing equation-based implementation and an actual SG. In contrast, this paper investigates the performance with different levels of detail in the SG's representation (e.g., different number of damper windings, etc.). It also develops small signal models of these representations and validates them using Electromagnetic Transients (EMT) simulation. In addition, the VSG configurations are investigated when connected to ac networks of different strengths - represented by short circuit ratios (SCR) - ranging from weak ($SCR < 2.0$) to ultra-strong ($SCR > 30$). Root locus analysis is carried out to investigate the stability and damping performance when the VSG representation uses different number of damper windings. Also, as the VSG parameters need not be constrained to the values of a physical machine, the use of artificially large parameters is investigated. It is shown that including damper windings inside the VSG results in a well-damped transient response.

This work was supported by the NSERC Canada.

C. Jiang, A. D. Sinkar, and A. M. Gole are with the Department of Electrical and Computer Engineering, University of Manitoba, Winnipeg, MB, R2T 5V6, Canada. (e-mail of corresponding author: jiangc38@myumanitoba.ca).

Paper submitted to the International Conference on Power Systems Transients (IPST2023) in Thessaloniki, Greece, June 12-15, 2023.

II. System Layout

The proposed VSG control method is tested in a VSC of the MMC type with 200 submodules (SMs) per arm. It is connected to an ac network with a short circuit ratio (SCR) of 4.5 as shown in Fig. 1.

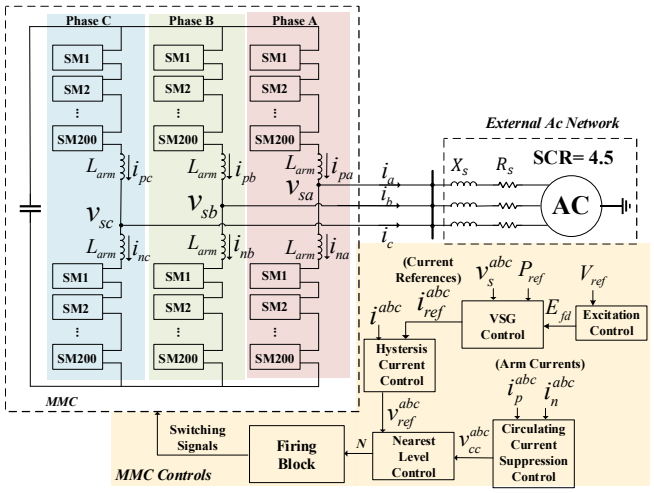

Fig. 1. Overall system layout and control diagram.

From the figure, the output variables of the proposed VSG controller are current references $i_{ref}^{abc} = [i_{ref}^{a}, i_{ref}^{b}, i_{ref}^{c}]$. With this, it is very easy to limit the current to a safe level, merely by limiting the magnitudes of i_{ref}^{abc}. The MMC's current controller block then generates the required voltage references v_{ref}^{abc} so that the MMC currents i^{abc} are essentially equal to i_{ref}^{abc}. Methods available to achieve this include the non-linear vector current source (NLVCS) control [15] and hysteresis current control [16] to name a few.

In hysteresis current control, the current is confined to a narrow envelope of width hy around the current reference i_{ref}. If the measured phase current is above the envelope (i.e., $i > i_{ref} + hy$), the output voltage is reduced to restore the current to be within the envelope. Similarly, if it is below the envelope, the voltage is increased. The method is widely used in two-level converters, but it has been adapted here for an MMC based on the approach of [16]. With this current controller, the MMC can be operated as a high-bandwidth and high-precision current source to generate any desired current waveforms.

In addition, a circulating current suppression controller (CCSC) is required to cancel circulating current harmonics in the MMC's arms [17]. It injects compensating voltages (v_{cc}^{abc}) which are added to the reference voltages v_{ref}^{abc} to produce the final voltage orders. Then, the firing block calculates the required number '*N*' of the activated submodules in each arm based on the voltage order and generates the necessary turn-on/turn-off commands for the appropriate submodules. In this paper, we use the commonly used 'nearest level control' (NLC) algorithm [17]. The objective of this paper is to achieve the behaviour of a real synchronous generator. The specific control strategy for generating i_{ref}^{abc} for this purpose is discussed below.

III. Current Controlled Virtual Synchronous Generator Control

A. Overall VSG controller

The structure of the proposed VSG controller is in Fig. 2. The VSG controller can be mainly divided into two parts, 1) Mechanical model and 2) Electrical equations, which exchange information with each other. The "Electrical equations" are used to generate the phase current references i_{ref}^{abc} using the SG equations as will be discussed later. An excitation controller is added to generate the field voltage (E_{fd}) based on the terminal voltage reference.

Current limiting is easily achieved by adding a maximum limit to the VSG's current orders i_d^{ref} and i_q^{ref} as shown in Fig. 2. Several limiter algorithms can be used for the GFM converter [18]. The circular magnitude limiter as shown in Fig. 3 is used in the examples in this paper to make sure the magnitude of the current reference $\sqrt{\left(i_{ref}^{d}\right)^2 + \left(i_{ref}^{q}\right)^2}$ is always below the allowed limit I_{MAX}, while the angle maintains the same.

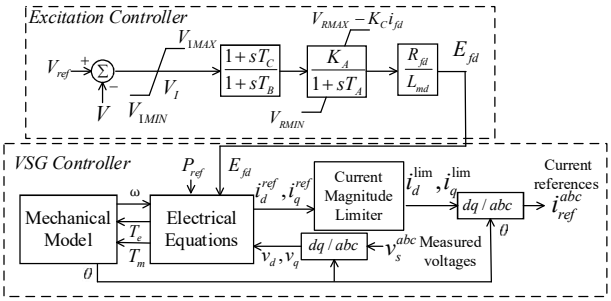

Fig. 2. Overall control structure.

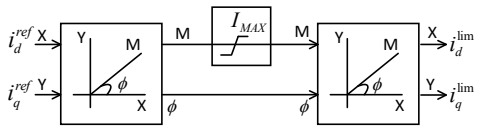

Fig. 3. Current magnitude limiter

Different models of SG with varying levels of modelling complexity are available in [19]. In the paper, we use the following:

1) An accurate representation with one damper winding each in the d- and q-axes

2) A less accurate representation without d- and q-axis damper windings.

Note that the only difference between these two VSG options is in the set of electrical equations.

B. Mechanical System Model

The mechanical modelling in the VSG controller contains the core swing equations of the SG as in (1) [19].

$$\begin{cases} 2H\frac{d\omega}{dt} = T_m - T_e - D_w\omega \\ \frac{d\theta}{dt} = \omega \\ T_m = \frac{P_{ref}}{\omega} + D_w\omega_0 \end{cases} \quad (1)$$

In (1), H is the inertia constant, P_{ref} is the active power reference, T_m is the mechanical torque and T_e is the

electromagnetic torque. The grid frequency and the machine's virtual angular speed are ω_0 and ω, respectively, while θ is the virtual rotor angle.

C. Electrical Equations

Two different electrical structures are shown in this section.

1) VSG Control with Damper Windings: The d- and q-axis equivalent circuits of this VSG controller are shown in Fig. 4. The model has a field winding and one damper winding (with currents i_{fd}, i_{1d}) on the d-axis whereas one damper winding (with currents i_{1q}) on the q-axis. The d and q-axis stator currents are i_d and i_q. Inductances L_a, L_{md}, L_{1d} etc., are the inductances of the various windings as shown in Fig. 4. The flux linkages of the respective windings are ψ_d, ψ_q etc., and 'p' is the time derivative operator e.g., $p\psi_d = d\psi_d/dt$, etc. The d- and q-axis components of the voltage are v_d and v_q. A detailed explanation of these equivalent circuits can be found in [19].

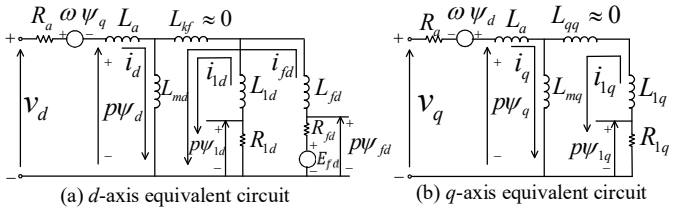

Fig. 4. Equivalent circuits of the VSG control with damper winding.

Based on Fig. 4, the relationships between currents and flux linkages are given in (2)-(6).

$$\psi_d = (L_a + L_{md})i_d + L_{md}i_{1d} + L_{md}i_{fd} \quad (2)$$

$$\psi_{1d} = L_{md}i_d + (L_{1d} + L_{md})i_{1d} + L_{md}i_{fd} \quad (3)$$

$$\psi_{fd} = L_{md}i_d + L_{md}i_{1d} + (L_{fd} + L_{md})i_{fd} \quad (4)$$

$$\psi_q = (L_a + L_{mq})i_q + L_{mq}i_{1q} \quad (5)$$

$$\psi_{1q} = L_{mq}i_q + (L_{1q} + L_{mq} + L_{qq})i_{1q} \quad (6)$$

The equations of voltages are given in (7)-(11).

$$\frac{d\psi_d}{dt} = v_d - i_d R_a - \omega\psi_q \quad (7)$$

$$\frac{d\psi_{1d}}{dt} = -R_{kd}i_{1d} \quad (8)$$

$$\frac{d\psi_{fd}}{dt} = E_{fd} - R_{fd}i_{fd} \quad (9)$$

$$\frac{d\psi_q}{dt} = v_q + \omega\psi_d - R_a i_q \quad (10)$$

$$\frac{d\psi_{1q}}{dt} = -R_{1q}i_{1q} \quad (11)$$

Using (2)-(11), the fluxes (ψ_d, ψ_q etc.) can be calculated by integration using a suitable numerical integration method (e.g., the trapezoidal rule) from which the currents (i_d, i_q etc.) are determined using (2)-(6). Also, the electromagnetic torque T_e required in (1) is calculated as in (12).

$$T_e = \psi_d i_q - \psi_q i_d \quad (12)$$

2) VSG Control Without Damper Winding: The d- and q-axis equivalent circuits of this VSG controller are shown in Fig. 5. Because of the similar structure, the electrical algorithm of this VSG controller without damper winding can also be obtained from (2)-(11) by simply dropping the terms related to damper winding currents (i_{1d} and i_{1q}). The equations are not repeated here.

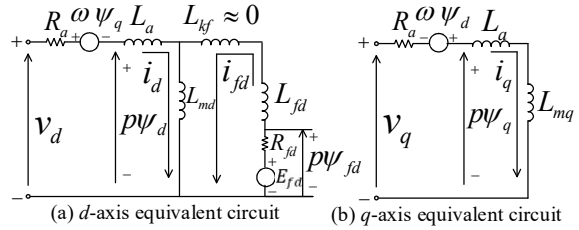

Fig. 5. Equivalent circuits of the VSG control without damper winding.

This also shows the proposed VSG controller is very flexible. The emulated electrical part can be modified easily by removing or adding corresponding flux/voltage equations without changing the existing equations. And the overall VSG structure keeps the same as in Fig. 2.

IV. Small Signal Model Of Proposed Virtual Synchronous Generator Control

Root locus analysis is widely used for studying the influence of the control parameters [11][13][19]. Before this, the small signal (SS) models of these control systems are required. The process of mathematically deriving the SS models is introduced in this section. These SS models are then validated using Electromagnetic Transients (EMT) simulation as shown in the next section.

A. SS Model of VSG Control with Damper windings

A small signal model is developed to analyze the effect of various parameters on the stability and dynamic behaviour of the VSG. The mathematical derivation is presented below.

1) SS model of the Electrical Equations: From (2)-(6), the small signal expressions of these linearized equations are in (13)-(15). 'T' represents the transpose of the matrix and the matrix $\boldsymbol{L_1}$ is given in the Appendix.

$$\Delta\boldsymbol{\psi_1} = \boldsymbol{L_1}\Delta\boldsymbol{I_1} \quad (13)$$

$$\Delta\boldsymbol{\psi_1} = \left(\Delta\psi_d \;\; \Delta\psi_{1d} \;\; \Delta\psi_{fd} \;\; \Delta\psi_q \;\; \Delta\psi_{1q}\right)^T \quad (14)$$

$$\Delta\boldsymbol{I_1} = \left(\Delta i_d \;\; \Delta i_{1d} \;\; \Delta i_{fd} \;\; \Delta i_q \;\; \Delta i_{1q}\right)^T \quad (15)$$

From (13), it is evident that:

$$\Delta\boldsymbol{I_1} = \boldsymbol{L_1^{-1}}\Delta\boldsymbol{\psi_1} \quad (16)$$

Also, converting (7)-(11) to their linearized equivalents, we get the flux differential equations as in (17)-(21). All the variables in per-unit (except 't' (time) which is measured in seconds). Here $\omega_n = 2\pi \times 60\, rad/s$ is the nominal virtual rotor speed ($60\, Hz$ system). The superscript '0' on any variable indicates that it is its steady-state value.

$$\frac{1}{\omega_n}\frac{d\Delta\psi_d}{dt} = \Delta v_d - R_a\Delta i_d - \omega^0\Delta\psi_q - \psi_q^0\Delta\omega \quad (17)$$

$$\frac{1}{\omega_n}\frac{d\Delta\psi_{1d}}{dt} = -R_{1d}\Delta i_{1d} \quad (18)$$

$$\frac{1}{\omega_n}\frac{d\Delta\psi_{fd}}{dt} = \Delta E_{fd} - R_{fd}\Delta i_{fd} \quad (19)$$

$$\frac{1}{\omega_n}\frac{d\Delta\psi_q}{dt} = \Delta v_q - R_a\Delta i_q + \omega^0\Delta\psi_d + \psi_d^0\Delta\omega \quad (20)$$

$$\frac{1}{\omega_n}\frac{d\Delta\psi_{1q}}{dt} = -R_{1q}\Delta i_{1q} \quad (21)$$

In the linearized differential equations above, the incremental flux linkages ($\Delta\psi_d$, $\Delta\psi_{1d}$, $\Delta\psi_{fd}$, $\Delta\psi_q$, $\Delta\psi_{1q}$) and the incremental field voltage (ΔE_{fd}) are state variables. The incremental currents (Δi_d, Δi_{1d}, Δi_{fd}, Δi_q, Δi_{1q}) can be re-written in terms of their corresponding flux linkages based on (16). Δv_d and Δv_q are not state variables but will be substituted later with state variables by using the equations of the interconnected external system.

2) SS model of Excitation Controller: From Fig. 2, the small signal model of the excitation control (ignoring the limits) is shown in Fig. 6, where $K_A' = K_A \cdot \frac{R_{fd}}{L_{md}}$. Two state variables ΔX_{E1} and ΔX_{E2} are introduced to represent the internal states of the first-order lag blocks as shown in Fig. 6.

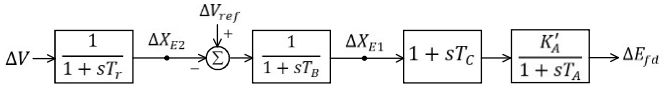

Fig. 6. Small signal model of excitation control.

In the dq reference frame, the voltage magnitude V is $\sqrt{v_d^2 + v_q^2}$. Hence, ΔV is as in (22), where V_l is the steady state magnitude of V as in (23).

$$\Delta V = \frac{v_d^0}{V_l}\Delta v_d + \frac{v_q^0}{V_l}\Delta v_q \quad (22)$$

$$V_l = \sqrt{(v_d^0)^2 + (v_q^0)^2} \quad (23)$$

Using Fig. 6, the small signal equations of the excitation controlled can be summarized as in (24)-(26). The units of the time constants (T_r, T_B, T_A) are in *seconds*.

$$\frac{d\Delta X_{E2}}{dt} = -\frac{1}{T_r}\Delta X_{E2} + \frac{v_d^0}{T_r V_l}\Delta v_d + \frac{v_q^0}{T_r V_l}\Delta v_q \quad (24)$$

$$\frac{d\Delta X_{E1}}{dt} = \frac{1}{T_B}\Delta V_{ref} - \frac{1}{T_B}\Delta X_{E1} - \frac{1}{T_B}\Delta X_{E2} \quad (25)$$

$$\frac{d\Delta E_{fd}}{dt} = -\frac{1}{T_A}\Delta E_{fd} + \frac{K_A'}{T_A}\left(1 - \frac{T_C}{T_B}\right)\Delta X_{E1} + \frac{K_A' T_C}{T_A T_B}\Delta V_{ref} - \frac{K_A' T_C}{T_A T_B}\Delta X_{E2} \quad (26)$$

3) SS model of the External System: The relationship between Δv_d, Δv_q and the state variables can be derived from the external power system which the converter connects to. The external system in Fig. 7 is equivalently represented as a Thevenin reactance X_s and a Thevenin voltage source $E_B\angle 0$. Any resistive component R_s, being much smaller than X_s, is ignored. The positive direction of the current phasor I is as shown in Fig. 7 and V_t is the converter's terminal voltage. From Fig. 7, (27) can be obtained.

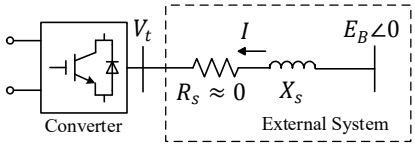

Fig. 7. Equivalent external power system.

$$V_t = V_R + jV_I = E_B - jX_sI = E_B + j0 - jX_s(I_R + jI_I) \quad (27)$$

Equation (27) is in the real-imaginary (RI) coordinates which rotate at the fundamental speed ($120\pi\ rad/s$ for a $60\ Hz$ system). This needs to be transformed into the dq reference frame (rotating at $\omega\ rad/s$) to be combined with the other VSG equations.

Fig. 8 shows that the q-axis lags the d-axis by 90°, and I-axis leads the R-axis by 90°. The angle between R-axis and d-axis is defined as δ and δ *is not* the rotor angle θ mentioned in (1). Then $\Delta\delta$, as given by (28) becomes one of the state variables.

$$\frac{1}{\omega_n}\frac{d\Delta\delta}{dt} = -\Delta\omega \quad (28)$$

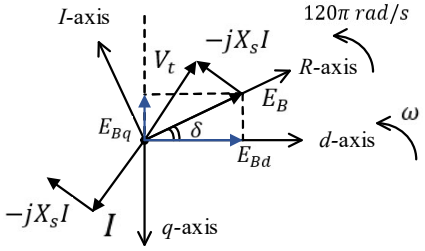

Fig. 8. Phasor relationship.

Also, the external system voltage E_B in dq reference frame can be obtained from Fig. 8 as shown in (29)-(30).

$$E_{Bd} = E_B \cdot cos\delta \quad (29)$$

$$E_{Bq} = -E_B \cdot sin\delta \quad (30)$$

Thus, (27) is rewritten in the dq frame as in (31)-(33).

$$v_d - jv_q = (E_{Bd} - jE_{Bq}) - jX_s(i_d - ji_q) \quad (31)$$

$$v_d = E_{Bd} - X_s i_q = E_B cos\delta - X_s i_q \quad (32)$$

$$v_q = E_{Bq} + X_s i_d = -E_B sin\delta + X_s i_d \quad (33)$$

Then, the incremental values of the d- and q-axis components of the voltage (Δv_d, Δv_q) are in (34) and (35). These are used to replace the voltages in (17), (20) and (24).

$$\Delta v_d = -E_B sin\delta^0 \cdot \Delta\delta - X_s\Delta i_q \quad (34)$$

$$\Delta v_q = -E_B cos\delta^0 \cdot \Delta\delta + X_s\Delta i_d \quad (35)$$

4) SS Model of the Mechanical Part: From (12), the expression for the incremental torque ΔT_e is in (36).

$$\Delta T_e = i_q^0\Delta\psi_d + \psi_d^0\Delta i_q - i_d^0\Delta\psi_q - \psi_q^0\Delta i_d \quad (36)$$

Then combining (1) and (36), the differential equation for $\Delta\omega$ can be written as in (37). As ΔT_m is approximately equal to ΔP_{ref} in the per-unit system, it is replaced by ΔP_{ref}. Also, the unit of the inertia constant H is *second*s.

$$\frac{d\Delta\omega}{dt} = \frac{\Delta P_{ref}}{2H} - \frac{D_w}{2H}\Delta\omega - \frac{i_q^0}{2H}\Delta\psi_d - \frac{\psi_d^0}{2H}\Delta i_q + \frac{i_d^0}{2H}\Delta\psi_q + \frac{\psi_q^0}{2H}\Delta i_d \quad (37)$$

Since the incremental rotor angle $\Delta\theta$ is only related to $\Delta\omega$ and is not used in other small signal differential equations, $\Delta\theta$ is neglected in the VSG small signal model.

5) Complete Small Signal Model: Combining the various components of the small signal model derived above, the complete set of small signal equations can be written in matrix form as in (38)-(42). Where, the '**0**' in (42) is the 5×5 zero matrix.

$$\frac{d\Delta \boldsymbol{x_1}}{dt} = \boldsymbol{A_1}\Delta \boldsymbol{x_1} + \boldsymbol{B_1}\Delta \boldsymbol{u} \quad (38)$$

$$\boldsymbol{A_1} = [\boldsymbol{M_1} + \boldsymbol{N_1}(\boldsymbol{L_1'})^{-1}] \quad (39)$$

$$\Delta \boldsymbol{x_1} = \left(\Delta\psi_d \ \Delta\psi_{1d} \ \Delta\psi_{fd} \ \Delta\psi_q \ \Delta\psi_{1q} \ \Delta\omega \ \Delta\delta \ \Delta E_{fd} \ \Delta X_{E1} \ \Delta X_{E2}\right)^T \quad (40)$$

$$\Delta \boldsymbol{u} = (\Delta P_{ref} \quad \Delta V_{ref})^T \quad (41)$$

$$\boldsymbol{L_1'} = \begin{pmatrix} \boldsymbol{L_1} & \boldsymbol{0} \\ \boldsymbol{0} & \boldsymbol{0} \end{pmatrix} \quad (42)$$

Matrices $\boldsymbol{M_1}$, $\boldsymbol{N_1}$ and $\boldsymbol{B_1}$ are given in the Appendix.

B. SS Model of VSG Control without Damper windings

The small signal model of the VSG controller without damper winding can be easily obtained by removing the corresponding differential equations related to the damper windings. Therefore, the matrix equation for the VSG without damper winding is as in (43) to (47).

$$\frac{d\Delta \boldsymbol{x_2}}{dt} = \boldsymbol{A_2}\Delta \boldsymbol{x_2} + \boldsymbol{B_2}\Delta \boldsymbol{u} \quad (43)$$

$$\boldsymbol{A_2} = [\boldsymbol{M_2} + \boldsymbol{N_2}(\boldsymbol{L_2'})^{-1}] \quad (44)$$

$$\Delta \boldsymbol{x_2} = \left(\Delta\psi_d \ \Delta\psi_{fd} \ \Delta\psi_q \ \Delta\omega \ \Delta\delta \ \Delta E_{fd} \ \Delta X_{E1} \ \Delta X_{E2}\right)^T \quad (45)$$

$$\boldsymbol{L_2} = \begin{pmatrix} L_a + L_{md} & L_{md} & 0 \\ L_{md} & L_{fd} + L_{kf} + L_{md} & 0 \\ 0 & 0 & L_a + L_{mq} \end{pmatrix} \quad (46)$$

$$\boldsymbol{L_2'} = \begin{pmatrix} \boldsymbol{L_2} & \boldsymbol{0} \\ \boldsymbol{0} & \boldsymbol{0} \end{pmatrix} \quad (47)$$

The matrices $\boldsymbol{M_2}$ and $\boldsymbol{N_2}$ are obtained by removing columns 2, and 5, as well as rows 2 and 5 of $\boldsymbol{M_1}$ and $\boldsymbol{N_1}$ respectively. Removing columns 2 and 5 from $\boldsymbol{B_1}$ gives $\boldsymbol{B_2}$.

V. Model Validation Using EMT Simulation

The proposed small signal (SS) models of the VSG controllers are validated by matching their transient responses with a fully detailed model in an EMT simulation program (PSCAD/EMTDC). The system layout for validation is the same as in Fig. 1, and its parameters are in Table I.

The SS model is linearized at the operating point where the output power of the MMC (P_t) is $1.0\ pu$. A step change in the active power reference ($\Delta P_{ref} = -0.1\ pu$) is applied in the EMT simulation as well as in the SS models.

Fig. 9 shows the transients of the virtual rotor speed obtained from the SS model ω_{SS} and EMT simulation ω_{EMT} of the proposed VSG with the damper windings. From Fig. 9, the traces are essentially overlapping and the maximum absolute error between these two curves is $1.39 \times 10^{-4}\ pu$ (as in Fig. 9 (b)) or $0.0139\ \%$ of the nominal value of ω_{EMT}. Thus, this validates the small signal model derived earlier.

The plot of the speed ω has an oscillatory component close to $1.85\ Hz$ and an attenuation constant close to $0.78\ s$. The curves show that the proposed control method is stable at the operating point as the speed ω recovers to $1.0\ pu$. This means the MMC synchronizes with the external ac system after the small disturbance.

Similarly, the accuracy of the SS model of the VSG control without damper windings can also be validated (not shown).

TABLE I
Main Parameters

Main System Parameters			
Parameter	Value	Parameter	Value
V_{dc}	$\pm 150\ kV$	f_{system}	$60Hz$
MMC S_{base}	$270\ MVA$	MMC V_{base}	$180kV$
System SCR	4.5	SMs per arm	200
Main VSG Control Parameters			
H	3.42 s	L_a	$0.015\ pu$
D_w	5.0	L_{md}	$2.0\ pu$
R_a	$0.0043\ \ pu$	L_{fd}	$0.119\ pu$
R_{1d}	$0.01823\ pu$	L_{1d}	$0.1097\ pu$
R_{1q}	$0.0104\ pu$	L_{1q}	$0.395\ pu$
R_{fd}	$0.0008947pu$	L_{mq}	$1.44pu$
Main Excitation Control Parameters			
T_C	$1.0\ s$	T_B	$10.0\ s$
K_A	200.0	T_A	$0.015\ s$
T_r	$0.02\ s$		

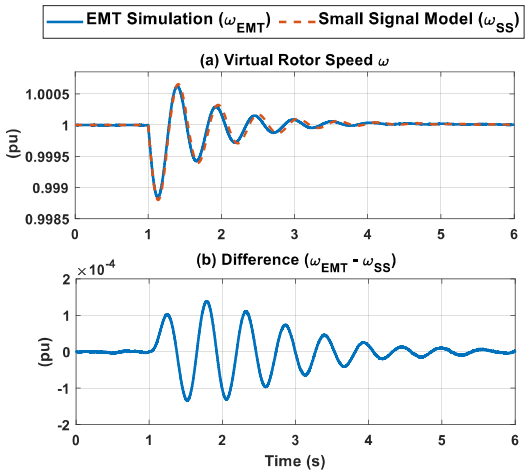

Fig. 9. SS model and EMT results of VSG control with damper windings.

VI. Root Locus Analysis

Root locus analysis is conducted on the small signal model for the operating point of $P_t = 1.0\ pu$ to investigate how the parameters of the ac system (X_s) as well as the damper windings (R_{1d}, L_{1d}, R_{1q}, L_{1q}) affect the stability and transient behaviour of the proposed VSG. The eigenvalues of matrix A_1 in (39) and A_2 in (44) can be plotted in the complex plane as a function of the parameters (e.g., X_s, R_{1d} etc.) being varied to generate a root locus plot from which the damping and the stability information can be garnered.

In this section, only the most critical eigenvalues close to the imaginary axis are plotted in the root loci.

A. VSG Performance under Varying System Strengths

Matrices A_1 and A_2 are functions of the ac system reactance X_s which is inversely proportional to SCR. Hence, root loci for varying SCR can be generated by varying X_s.

Fig. 10 (a) and (b) respectively show the plot of the critical eigenvalues of A_1 (X) and A_2 (O), as the SCR varies from $SCR = 1.2$ for a weak system to $SCR = 100$ for an ultra-stiff system. Other non-varying parameters are given in Table I. As the eigenvalues have negative real parts, both VSG options exhibit stable operation over the entire SCR range.

This indicates a performance enhancement compared with previous VSGs that utilize embedded current controllers which may become unstable with high SCR ac systems [13]. This could be attributed to the delays inherent in the proportional-integral (PI) controller. In contrast, the proposed VSG uses a hysteresis current controller to generate the currents which is extremely rapid with minimal delay.

Additionally, from Fig. 10, an increase in the SCR for the VSG model leads to a shift of the oscillatory eigenvalues to the left, which indicates an improvement in the damping of oscillations. For example, the damping ratio (ξ), when the damper windings are included, is 0.059 for $SCR = 1.2$ and $\xi = 0.159$ for $SCR = 20$. Also, there is an increase in the oscillation frequency (f_n) with a larger SCR. For example, f_n, when the damper windings are included, is $1.07\,Hz$ for $SCR = 1.2$ and $f_n = 2.56\,Hz$ for $SCR = 20$.

The step responses of ω with $\Delta P_{ref} = -0.1\,pu$ in Fig. 11 is consistent with the above conclusions. For example, measurements from the waveforms show that $\xi = 0.067$ and $f_n = 0.93\,Hz$ for $SCR = 1.2$, whereas $\xi = 0.155$ and $f_n = 2.53\,Hz$ for $SCR = 20$. These values match the information obtained from the SS model. Similar conclusions can also be drawn from the transient waveforms of the VSG with no damper windings, which is omitted here for brevity.

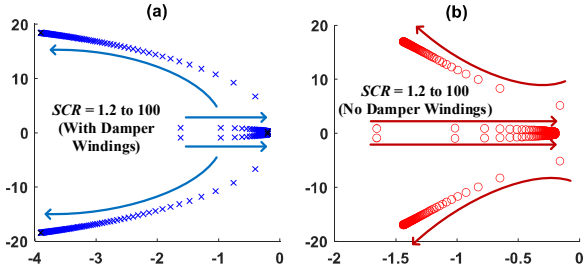

Fig. 10 Root loci with SCR increasing. (a) VSG1 (with damper windings) (b) VSG2 (without damper windings).

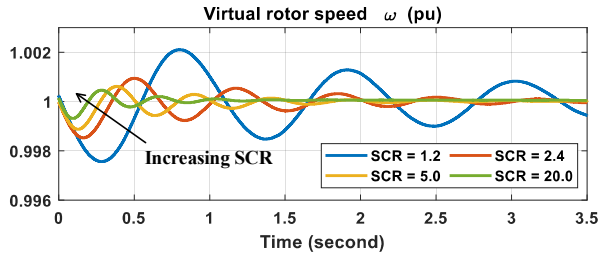

Fig. 11 Step responses for VSG1 (with damper windings) with different SCR Systems.

B. VSG Performance with Varying Damper Resistance R_{1d}

Fig. 12 shows the plot of the eigenvalues of A_1 (indicated by X), as the d-axis damper resistance R_{1d} changes from $0.0\,pu$ to $1.0\,pu$. Other non-varying parameters are given in Table I. The eigenvalues of A_2 are also shown in the same plot (represented by O), which remain stationary as the damper windings are not included in A_2.

The eigenvalues of A_1 move asymptotically towards the eigenvalues of A_2 as R_{1d} increases, which is to be expected as having no damper winding is tantamount to having a damper winding with $R_{1d} = \infty$. As can be seen, the operation is stable over the entire range of R_{1d}.

A zoomed in plot of the oscillatory eigenvalues is shown in the right-hand frame in Fig. 12. The oscillation frequency is largely unchanged at around $11.8\,rad/s$ ($1.85\,Hz$). The VSG controller with no damper windings has the least damping ratio of 0.084 for the dominant oscillatory mode. While with the damper winding, the real part of the oscillatory eigenvalues first increases with increasing R_{1d}, attains a maximum for $R_{1d} = 0.008\,pu$ and then decreases. Thus, in this example, the largest damping ratio of 0.119 occurs for $R_{1d} = 0.008\,pu$. Hence, including the damper windings in the VSG does improve the damping ratio from 0.084 to 0.119.

The above conclusions can be validated using a time domain simulation. Fig. 13 shows step responses of ω with $\Delta P_{ref} = -0.1\,pu$ for three cases: i) VSG with no damper winding, ii) VSG with $R_{1d} = 0.008\,pu$, and iii) VSG with $R_{1d} = 0.1823\,pu$. As expected, damping ratio of the oscillatory mode is the largest for $R_{1d} = 0.008\,pu$ ($\xi = 0.121$) while it is the least ($\xi = 0.086$) for the controller without any damper windings. This is in excellent agreement with the values $\xi = 0.119$ and $\xi = 0.084$ obtained from the SS analysis. The oscillation frequencies vary marginally, being $1.95\,Hz$ for $R_{1d} = 0.008\,pu$, $1.86\,Hz$ for $R_{1d} = 0.1823\,pu$ and $1.83\,Hz$ for the no damper winding case, which also agrees with the SS analysis results.

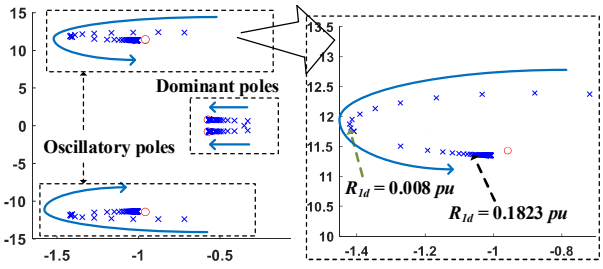

Fig. 12. Root loci with R_{1d} increasing.

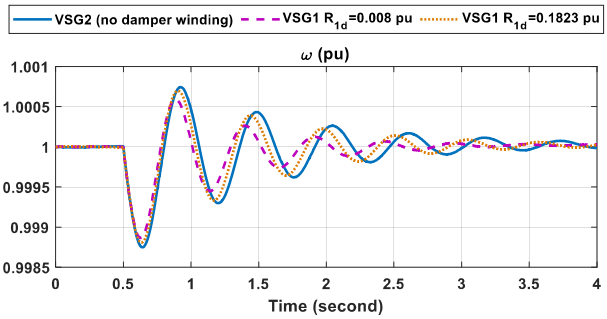

Fig. 13. Simulation waveforms showing R_{1d} effect.

C. VSG Performance with Varying Damper Inductance L_{1d}

Fig. 14 shows the plot of the eigenvalues of A_1 (X), as the d-axis damper inductance L_{1d} changes from $0.0\,pu$ to $10.0\,pu$. One of the dominant poles is zoomed in and shown on the right. The eigenvalues of A_2 (O) are also plotted and remain stationary as the formulation of A_2 does not include L_{1d}. Additionally, Fig. 15 shows the step responses of ω with $\Delta P_{ref} = -0.1\,pu$ for three cases, viz. i) VSG with no damper

winding, ii) VSG with $L_{1d} = 0.01\,pu$, and iii) VSG with $L_{1d} = 1.097\,pu$.

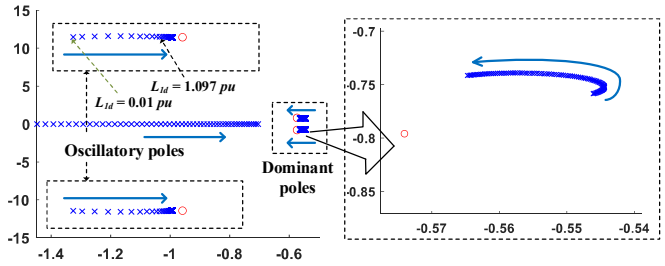

Fig. 14. Root loci with L_{1d} increasing.

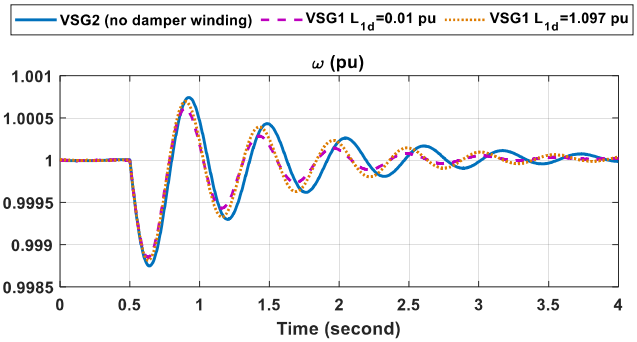

Fig. 15. Simulation waveforms showing L_{1d} effect.

From the zoomed-in plot of Fig. 14, the dominant pole first moves closer to and then turns away from the imaginary axis. Therefore, the worst operating situation from the point of view of system stability happens at the furthest right of the root locus, where L_{1d} is around $2.5\,pu$.

Observing the oscillatory poles in Fig. 14, the VSG controller without damper windings has the least damping ratio (ξ) which is 0.084. For VSG with damper windings, a smaller L_{1d} gives better damping, for example $\xi = 0.114$ for $L_{1d} = 0.01\,pu$. Also, the oscillation frequency is unchanged at around $1.83\,Hz$ with varying L_{1d}.

The EMT simulation in Fig. 15 confirms the root locus results. The VSG with $L_{1d} = 0.01\,pu$ has the most damped response which is measured to be $\xi = 0.118$ and the least transient settling time. In contrast, the damping ratio is the smallest for the VSG without damper windings, and measurement gives it as 0.086. These results match the information ($\xi = 0.114$ and $\xi = 0.084$) obtained from the SS analysis. It can be seen that the transient performance is marginally improved with the inclusion of the damper windings.

The root loci (not shown here) obtained by varying the q-axis damper resistance and inductance (R_{1q} and L_{1q}) are qualitatively similar, as those with varying R_{1d} and L_{1d}.

VII. Conclusions

In this paper, a novel detailed synchronous machine emulation VSG control approach is introduced. The MMC interfaces to the network as a current source, with the current references being calculated using the full set of equations representing a synchronous generator. The proposed VSG control is flexible, as the number of windings as well as the winding parameters can be changed. Two VSG controllers with different modeling complexity based on SG structure are developed, one with, and the other without representing the damper windings.

Small signal analysis, validated using EMT simulation, shows that with or without the damper windings, the overall VSG model remains stable not only in weak systems, but also in ultra-stiff systems, which was identified as a challenge for earlier VSG implementations. Also, for a given ac system, the d- and q-axis damper winding impedances in the model can be optimized to provide maximum damping and marginally improve the transient performance. From the view of modeling complexity and tuned parameters, the simplified VSG without any damper winding is easier to implement and tune as it has a smaller number of parameters.

VIII. Appendix

Matrices $\boldsymbol{M_1}$, $\boldsymbol{N_1}$, $\boldsymbol{L_1}$, and $\boldsymbol{B_1}$ are given in (A-1) to (A-4) in this section.

$$\boldsymbol{M_1} = \begin{pmatrix} 0 & 0 & 0 & -\omega^0\omega_n & 0 & -\psi_q^0\omega_n & -E_B sin\delta^0\omega_n & 0 & 0 & 0 \\ 0 & 0 & 0 & 0 & 0 & 0 & 0 & 0 & 0 & 0 \\ 0 & 0 & 0 & 0 & 0 & 0 & 0 & \omega_n & 0 & 0 \\ \omega^0\omega_n & 0 & 0 & 0 & 0 & \psi_d^0\omega_n & -E_B cos\delta^0\omega_n & 0 & 0 & 0 \\ 0 & 0 & 0 & 0 & 0 & 0 & 0 & 0 & 0 & 0 \\ -\frac{i_q^0}{2H} & 0 & 0 & \frac{i_d^0}{2H} & 0 & -\frac{D_w}{2H} & 0 & 0 & 0 & 0 \\ 0 & 0 & 0 & 0 & 0 & -\omega_n & 0 & 0 & 0 & 0 \\ 0 & 0 & 0 & 0 & 0 & 0 & 0 & -\frac{1}{T_A} & \frac{K_A'}{T_A}(1-\frac{T_C}{T_B}) & -\frac{K_A' T_C}{T_A T_B} \\ 0 & 0 & 0 & 0 & 0 & 0 & 0 & 0 & -\frac{1}{T_B} & -\frac{1}{T_B} \\ 0 & 0 & 0 & 0 & 0 & 0 & \frac{-E_B v_d^0 sin\delta^0 - E_B v_q^0 cos\delta^0}{T_r V_l} & 0 & 0 & -\frac{1}{T_r} \end{pmatrix} \quad \text{(A-1)}$$

$$\boldsymbol{N_1} = \begin{pmatrix} -R_a\omega_n & 0 & 0 & -X_s\omega_n & 0 & 0 & 0 & 0 & 0 & 0 \\ 0 & -R_{1d}\omega_n & 0 & 0 & 0 & 0 & 0 & 0 & 0 & 0 \\ 0 & 0 & -R_{fd}\omega_n & 0 & 0 & 0 & 0 & 0 & 0 & 0 \\ X_s\omega_n & 0 & 0 & -R_a\omega_n & 0 & 0 & 0 & 0 & 0 & 0 \\ 0 & 0 & 0 & 0 & -R_{1q}\omega_n & 0 & 0 & 0 & 0 & 0 \\ \frac{\psi_q^0}{2H} & 0 & 0 & -\frac{\psi_d^0}{2H} & 0 & 0 & 0 & 0 & 0 & 0 \\ 0 & 0 & 0 & 0 & 0 & 0 & 0 & 0 & 0 & 0 \\ 0 & 0 & 0 & 0 & 0 & 0 & 0 & 0 & 0 & 0 \\ 0 & 0 & 0 & 0 & 0 & 0 & 0 & 0 & 0 & 0 \\ \frac{v_q^0}{T_r V_l} X_s & 0 & 0 & -\frac{v_d^0}{T_r V_l} X_s & 0 & 0 & 0 & 0 & 0 & 0 \end{pmatrix} \tag{A-2}$$

$$\boldsymbol{L_1} = \begin{pmatrix} L_a + L_{md} & L_{md} & L_{md} & 0 & 0 \\ L_{md} & L_{kd} + L_{kf} + L_{md} & L_{kf} + L_{md} & 0 & 0 \\ L_{md} & L_{kf} + L_{md} & L_{fd} + L_{kf} + L_{md} & 0 & 0 \\ 0 & 0 & 0 & L_a + L_{mq} & L_{mq} \\ 0 & 0 & 0 & L_{mq} & L_{1q} + L_{qq} + L_{mq} \end{pmatrix} \tag{A-3}$$

$$\boldsymbol{B_1} = \begin{pmatrix} 0 & 0 & 0 & 0 & 0 & \frac{1}{2H} & 0 & 0 & 0 & 0 \\ 0 & 0 & 0 & 0 & 0 & 0 & 0 & \frac{K_A T_C}{T_A T_B} & \frac{1}{T_B} & 0 \end{pmatrix}^T \tag{A-4}$$

IX. References

[1] J. Arrillaga, *High Voltage Direct Current Transmission*, 2nd Edition. London: The Institution of Electrical Engineers, 1998.

[2] A. Yazdani and R. Iravani, "*Voltage-sourced Converters in Power Systems: Modeling, Control, and Applications*." John Wiley & Sons, 2010.

[3] M. Glinka and R. Marquardt, "A new AC/AC multilevel converter family," *IEEE Transactions on Industrial Electronics*, vol. 52, no. 3, pp. 662-669, June 2005

[4] S. Debnath, J. Qin, B. Bahrani, M. Saeedifard and P. Barbosa, "Operation, Control, and Applications of the Modular Multilevel Converter: A Review," *IEEE Transactions on Power Electronics*, vol. 30, no. 1, pp. 37-53, Jan. 2015

[5] M. Hiller, D. Krug, R. Sommer and S. Rohner, "A new highly modular medium voltage converter topology for industrial drive applications," in *13th European Conference on Power Electronics and Applications*, 2009, pp. 1-10

[6] S. Debnath and M. Saeedifard, "A New Hybrid Modular Multilevel Converter for Grid Connection of Large Wind Turbines," *IEEE Transactions on Sustainable Energy*, vol. 4, no. 4, pp. 1051-1064, Oct. 2013

[7] J. H. Vivas, G. Bergna and M. Boyra, "Comparison of multilevel converter-based STATCOMs," in *14th European Conference on Power Electronics and Applications*, 2011, pp. 1-10

[8] H. Zhang, W. Xiang, W. Lin and J. Wen, "Grid Forming Converters in Renewable Energy Sources Dominated Power Grid: Control Strategy, Stability, Application, and Challenges," *Journal of Modern Power Systems and Clean Energy*, vol. 9, no. 6, pp. 1239-1256, November 2021.

[9] Q.-C. Zhong and G. Weiss. ' Synchronverters: Inverters that mimic synchronous generators', *IEEE Trans. Ind. Electron*., 2011, 58, (4), pp. 1259–1267

[10] J. Roldán-Pérez, A. Rodríguez-Cabero and M. Prodanovic, "Design and Analysis of Virtual Synchronous Machines in Inductive and Resistive Weak Grids," *IEEE Transactions on Energy Conversion*, vol. 34, no. 4, pp. 1818-1828, Dec. 2019.

[11] Salvatore D'Arco, Jon Are Suul, Olav B. Fosso, "A Virtual Synchronous Machine implementation for distributed control of power converters in SmartGrids", *Electric Power Systems Research*, Volume 122, 2015, Pages 180-197, ISSN 0378-7796

[12] P. Rodríguez, C. Citro, J. I. Candela, J. Rocabert and A. Luna, "Flexible Grid Connection and Islanding of SPC-Based PV Power Converters," *IEEE Transactions on Industry Applications*, vol. 54, no. 3, pp. 2690-2702, May-June 2018

[13] A. F. Darbandi, A. Sinkar and A. Gole, "Effect of Short-Circuit Ratio and Current Limiting on the Stability of a Virtual Synchronous Machine Type Gridforming Converter," in *17th International Conference on AC and DC Power Transmission (ACDC 2021)*, Glasgow, UK, 2021, pp. 182-187.

[14] C. Jiang, A. D. Sinkar and A. M. Gole, "Comparative study of Swing Equation-based and full emulation-based Virtual Synchronous Generators," in *11th International Conference on Power Electronics, Machines and Drives (PEMD 2022),* 2022, pp. 578-582.

[15] F. Martinez-Rodrigo, D. Ramirez, H. Mendonça, S. de Pablo, "MMC as nonlinear vector current source for grid connection of wave energy generation", *International Journal of Electrical Power & Energy Systems*, Volume 113, 2019, Pages 686-698

[16] L. Yunbo, X. Yonghai and X. Yunfei, 'A MMC hysteresis current control method based on current slope', in *IECON 2017 - 43rd Annual Conference of the IEEE Industrial Electronics Society*, 2017, pp. 577-582

[17] Sharifabadi, Kamran, et al. "*Design, control, and application of modular multilevel converters for HVDC transmission systems*". John Wiley & Sons, 2016

[18] B. Fan, T. Liu, F. Zhao, H. Wu and X. Wang, "A Review of Current-Limiting Control of Grid-Forming Inverters Under Symmetrical Disturbances," *IEEE Open Journal of Power Electronics*, vol. 3, pp. 955-969, 2022.

[19] P. Kundur, N. J. Balu, and M. G. Lauby.: ' *Power System Stability and Control* ' (McGraw-hill New York, 1997, vol. 7).